

# Corrosion Study Of Inconel 625 Coating Deposited By TIG Welding On AISI 4130 Steel

Élida M.A. Alves<sup>1</sup>, Igor A. Fioravante<sup>1</sup>, Rafael R. Lucas<sup>1</sup>,  
Rosinei Batista Ribeiro<sup>2</sup>, Peterson L. Ferrandini<sup>1</sup>, Heloísa A. Acciari<sup>1</sup>,  
Roberto Z. Nakazato<sup>1</sup>, Eduardo N. Codaro<sup>1</sup>

*Faculdade De Engenharia E Ciências De Guaratinguetá, Universidade Estadual Paulista “Júlio De Mesquita Filho” (UNESP), Guaratinguetá, SP, Brasil.*

*Centro Estadual De Educação Tecnológica Paula Souza - Unidade De Pós - Graduação, Extensão E Pesquisa (CEETEPS - UPEP), São Paulo, SP, Brasil.*

---

## **Abstract:**

*Superalloy Inconel 625 is widely used in the oil and gas industry as an internal coating for pipes and valves due to its resistance to corrosion. The objective of this work was to investigate the behavior of the Inconel 625 coating, deposited by TIG welding on AISI 4130 steel, in NACE TM0177 solution. Microstructural and chemical analysis of the coating revealed a disordered growth of columnar and equiaxed dendrites and a high iron content throughout its thickness. Electrochemical tests were carried out under three different conditions: i) naturally aerated, ii) deaerated with a constant flow of nitrogen gas and iii) deaerated with a constant flow of hydrogen sulfide gas at room temperature. In the first two conditions, the results revealed a complex behavior, highlighting very low passive current densities, probably due to the formation of a thin and adherent film on the surface of the coating. In the last condition, measurements indicate a strong surface attack with dissolution of corrosion products.*

**Keywords:** *Inconel 625, TIG welding, Metallic coating, Corrosion.*

---

Date of Submission: 25-04-2025

Date of Acceptance: 05-05-2025

---

## I. Introduction

Many low-alloy carbon steels, which have high mechanical strength, formability and low cost, are used in pipelines. used in oil pipelines. Hydrogen sulphide, which is naturally present in oil, together with present in oil, together with emulsified water and water vapor, make the acidic environment environment conducive to corrosion, known as sour [1,2]. Corrosion of these pipelines creates an environmental safety problem, and their inspection and repair are economically costly due to the operational infrastructure and production downtime. downtime. In order to mitigate this problem, nickel-based alloys are often used to coat the internal surfaces of pipeline connectors and valves [3,4] due to their good weldability and resistance to corrosion [5,6]. corrosion [5,6]. Today, welding has become a joining process, and repair process that is versatile, efficient and affordable. O welding can be achieved by various processes, such as coated electrodes, TIG, MIG/MAG, cored wire, explosion and plasma, but TIG is the most widely process because it is easier to control the conditions of the weld pool, although there is research that shows that it is possible to use the other methods to reduce scrap and rework costs. There are different types of nickel-based nickel-based alloys, one of the most widely used in the industrial sector being Inconel 625. is Inconel 625. However, some problems can arise during the deposition of Inconel 625 by welding. The elements Nb and Mo, for example, can be segregated into the liquid, resulting in greater dilution of iron from the substrate in the weld pool. in the weld pool [7,8,3,4]. The heat input and the dilution play an important role in the microstructure. In TIG welding, low heat input values lead to a lower tendency of carbon diffusion of carbon towards the coating and inhibition of the formation during the deposition of Inconel 625 on low-alloy steels [9,10].

The electrochemical behavior of Inconel 625 is complex due to the high content of alloying elements such as Ni, Mo, Nb and Cr. Mo and Nb in solid solution improve the mechanical strength of the alloy; Cr and Mo increase corrosion resistance and Nb reduces intergranular corrosion through the formation of carbides. To be used in the oil industry, Inconel 625 must have a maximum Fe content in the coating of 10% measured 3 mm from the surface of the substrate or base metal [6, 8, 11]. The corrosion resistance of Inconel 625 deposited by welding is directly associated with its microstructure, occurring mainly in the interdendritic region, where the protection of the passive film is lower due to the decrease in Ni and Cr [12]. According to Mohammadi and

Alfantazi [13], the mechanism of localized corrosion in Inconel 625 coatings is related to galvanic corrosion between the interdendritic region and the dendritic core. In this context, the aim of this work was to analyze the microstructure and corrosion resistance of Inconel 625 alloy, deposited by TIG welding on AISI 4130 steel, in NACE TM0177 solution [14]. This standard establishes test conditions in acidic media for low-alloy carbon steels with relatively high resistance to cracking. It covers four SSC (sulfide stress cracking)/SCC (Stress Corrosion Cracking) test methods designated A: Uniaxial Tension; B: Curved Beam; C: C Ring and D: Double Cantilever Beam, and details environments and procedures, not providing acceptance levels or pass/fail criteria.

## II. Materials And Methods

Inconel 625 in the form of a 1.2 mm diameter rod was deposited by the TIG process on a 130 x 30 x 15 mm AISI 4130 steel plate (base metal - MB). The chemical composition of the rod and the steel is shown in Table 1.

**Table 1:** Nominal chemical composition of AISI 4130 steel and Inconel 625 (% by mass) [15].

Element		Mn	Si	Cr	Ni	Mo	Nb	Co	Al	Ti	Fe
ANSI 4130	Min	0.28	0.40	0.15	0.80	-	0.15	-	-	-	bal
	Max	0.33	0.30	0.30	1.10	0.50	0.25	-	-	-	bal
Inconel 625	Min	-	-	-	20.0	60.0	8.0	3.15	-	-	-
	Max	0.1	0.50	0.50	23.0	bal	10.0	4.15	1.0	0.40	0.40

Manual welding was carried out in a flat position with a 45° inclination between the Inconel rod and the substrate surface, under an argon atmosphere. A layer was deposited on the steel and the coated plate was cooled to room temperature. The welding parameters used are listed in Table 2 [13]. In order to avoid excessive martensite formation, cracks and distortion of the substrate, the AISI 4130 steel plate was preheated in an oven to a temperature of 135°C before being deposited by welding.

**Table 2.** Parameters used in welding.

Parameters	Values
Welding Current	130A
Welding Voltage	13 V
Welding Speed	117 mm/min
Thermal Input	0,693 kj/mm
Gas Flow	15L/mm

In order to calculate the thermal support, it was required to know the arc power, which in turn was obtained from the values of the welding current and the welding speed. The thermal input (HI) was calculated using equation (1), in which I = welding current (A), V = arc voltage, S = welding speed (mm/min) and η = thermal efficiency (%). In the TIG welding process case, the thermal efficiency was 80% [13].

$$HI = \eta \times \frac{I \times V}{S}, J/mm \quad (1)$$

After welding, the specimens (Figure 1) were cut according to the specifics of each test. For metallographic analysis, one specimen was hot dipped, mechanically sanded with 100, 220, 320, 400, 600, 1200 and 2400 mesh sandpaper, polished with colloidal silica suspension and diamond paste (6, 3 and 1 μm) ASTM E 3, 2017 [16].

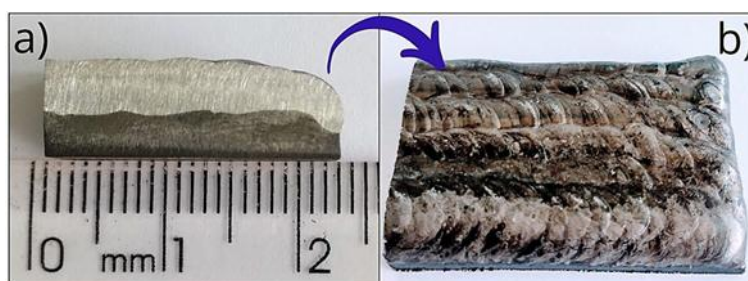


**Fig 1.** Specimen: a) side view and b) top view.

The microstructure of the specimen was revealed by immersion in a solution consisting of: HNO<sub>3</sub> (50 mL), HCl (45 mL) and H<sub>2</sub>O<sub>2</sub> (5 mL) for 20 s. The images shown were obtained using brightfield optical microscopy (OM) and scanning electron microscopy (SEM).

The chemical compositions of the samples used, shown in Table 3, were obtained by energy dispersive x-ray spectroscopy (EDS) using a HITACHI TM3000® electron microscope. The morphology of the coating, the thermally affected zone (HAZ) and the molten zone (MZ) were studied. In order to characterize the behavior and quality of the weld along its entire length, 15 Vickers microhardness measurements were taken, 5 in the MB, 5 in the HAZ and 5 in the FZ, using a Wilson Instruments Model 401 MVD® microhardness tester with a load of 300 gf and an application time of 15s (ASTM E384, 2016) [17].

To study the corrosion, open-circuit potential measurements were taken followed by the recording of potentiodynamic polarization curves at a scan rate of 0.166 mV/s. The electrochemical cell consisted of a borosilicate glass tube, closed at the ends by polyacetal plates, into which a test specimen like the one in Figure 1a (now addressed as the work electrode) and an Ag/AgCl, KCl sat. reference electrode was fitted, both connected to an AutoLab PGSTAT302 potentiostat. A spiral-shaped Pt counter electrode was connected to the other terminal of the potentiostat (Figure 2). Solution A of the NACE TM 0177 standard [14], consisting of 5.0 NaCl and 0.5% CH<sub>3</sub>COOH (by mass), was used as the electrolyte. The initial pH varied between 2.6 and 2.8 and the final pH after the corrosion test was less than 4.0, as indicated in this standard.

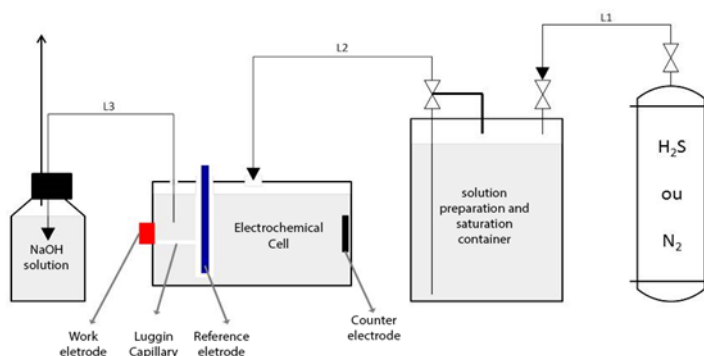


Fig 2. Illustration of the device for electrochemical measurements.

Before each measurement, the sample was sanded using 100, 220, 320, 400 and 600 mesh sandpaper. With each change of sandpaper, care was taken to rotate the sample by 90° in order to eliminate all scratches from the previous sanding. Afterwards, the samples were rinsed with distilled water and then with isopropyl alcohol, and the drying process was completed with a blast of cold air. The tests were carried out under three experimental conditions: i) aerated at room temperature and atmospheric pressure; ii) deaerated with constant circulation of N<sub>2</sub> (g) at room temperature; deaerated with constant circulation of N<sub>2</sub>(g) for one hour and then saturated with H<sub>2</sub>S(g) at room temperature. A container containing 20% NaOH by mass was used to neutralize the H<sub>2</sub>S and reduce emissions into the atmosphere, since this gas is flammable and toxic.

### III. Results And Discussion

#### Microstructural analysis and hardness values

The microstructures found by means of MO and SEM of the coating and the interface between the coating and the substrate are an important characteristic of manual TIG welding. Figure 3 shows the microstructure of the deposited coating layer, which is completely dendritic as a result of the solidification process observed. Note that the dendrites do not show a preferential direction of growth, which suggests that the heat extraction during the solidification process was irregular, consistent with the deposition carried out using the manual TIG welding process. Similar results have been reported by other authors [18, 19].

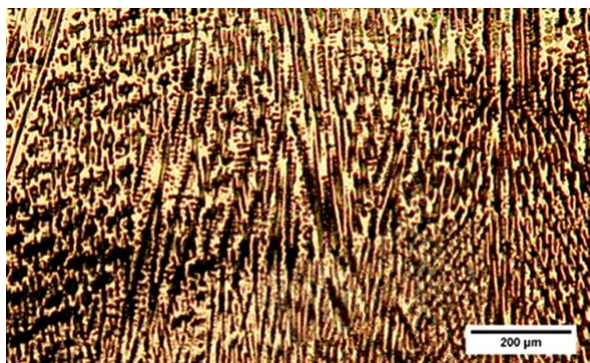


Fig 3. Microstructure of the coating showing disordered dendritic growth.

Figure 4 shows the microstructure of standardized AISI 4130 type "F" steel, consisting of ferrite grains of different shapes and sizes (light region) and pearlite (dark region), which has a homogeneous appearance and significantly defined grain boundaries.

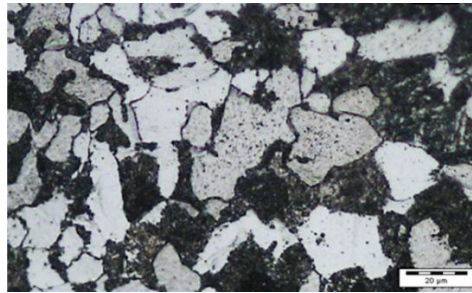


Fig 4. Microstructure of AISI 4130 steel "as received".

Figure 5 shows the microstructure of the steel after welding. The width of the thermally affected zone (HAZ), measured from the interface with the coating (bottom right) is approximately 1350 μm. Note that near the substrate/coating interface the microstructure is martensitic, due to the relatively rapid cooling after deposition. At the other end (top left) the microstructure is ferritic pearlitic, as in figure 4. The HAZ can be considered large, which is attributed to the preheating applied to the substrate. The result found is consistent with results reported by other authors [20, 21].

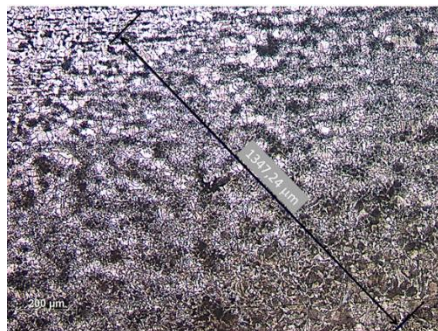


Fig 5. Microstructure of SAE 4130 steel after welding.

Figure 6a shows in yellow the coating-substrate interface (FZ) with no defined morphology. In this zone, the solidification process takes place through the mechanisms of nucleation and growth of new phases from a solid-liquid interface. The EDS analysis of this region shows high concentrations of Ni, Cr and Fe (Figure 6b), the first two coming mainly from the rod and the last from the steel, in accordance with Table 1.

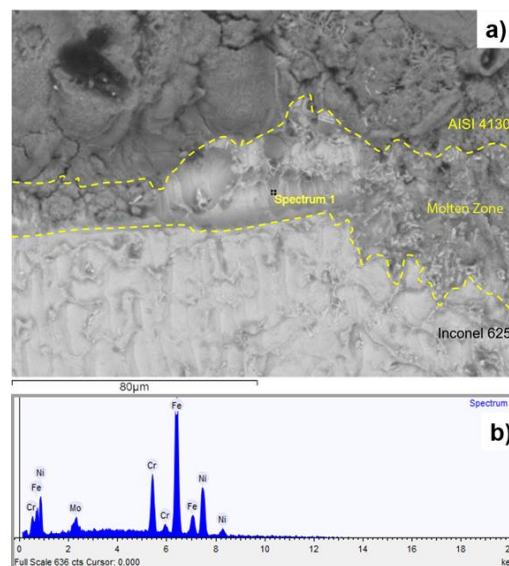


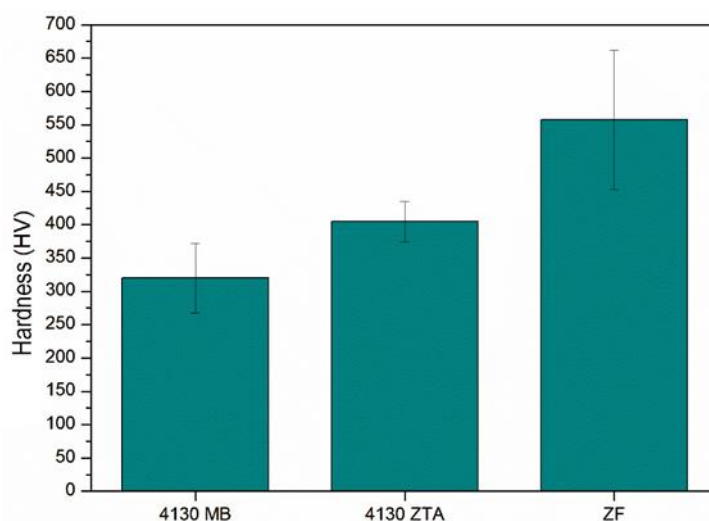
Fig 6. Interface: a) SEM of the cross-section and b) EDS at the location marked "+ Spectrum 1".

The compositions were determined throughout the thickness of the specimen, i.e. on the substrate, at the interface and in the coating (Table 3). The high Fe content and the increase in the Cr/Ni ratio at the interface (Cr enrichment) stand out, which shows the dissolution of the substrate and the dilution expected in a welding process. The higher Fe contents found at greater distances from the interface can be attributed to the segregation of Fe during the solidification of the coating. In the region closest to the interface, there is a significant Fe content (20.21% at the +0.5 mm position), then a drop (18.67% at +1 mm) and then an upward trend. A possible explanation for this behavior could be the decrease in solidification speed with greater segregation of Fe into the liquid, resulting in a higher content of the element near the surface (+2 mm), the last region to solidify. This suggests increasing the reinforcement of coatings in welding processes that impose high levels of dilution, requiring more than one layer to ensure that the chemical composition of the coating has minimal iron contamination from the substrate.

**Table 3.** Chemical composition throughout the thickness of the specimen (% by mass).

Element	Fe	Ni	Cr	Mo
-0,5 mm (in the subtract)	97,25	0,28	1,25	-
0,0 mm (at the interface)	82,0	10,68	5,22	1,01
+0,5 mm (in the coating)	20,21	50,3	21,13	5,19
+1,0 mm (in the coating)	18,67	53,81	22,19	4,78
+1,5 mm (in the coating)	23,03	48,13	20,50	5,03
+2,0 mm (in the coating)	24,58	48,93	20,82	4,46

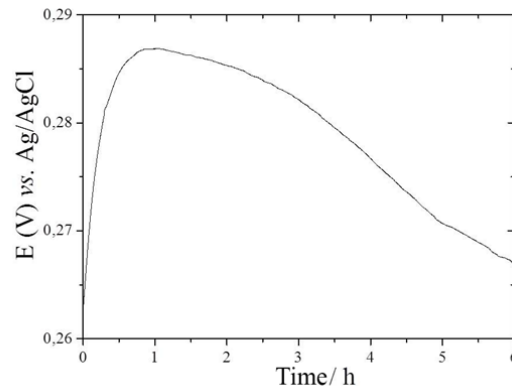
The hardness values observed in the three regions of the samples, obtained by Vickers microhardness, show significant variations, particularly in the fused zone (FZ) (Figure 7). It can be seen that the standard deviation values are significantly higher in the FZ and also that the average hardness value observed in the FZ is higher than that observed in the HAZ, which has a martensitic structure. The relatively low hardness value found in the HAZ was attributed to the fact that the substrate was a low carbon AISI 4130 steel, which generates relatively low hardness martensite, while the relatively high hardness value shown by Inconel in the FZ was attributed to the enrichment of Fe and Cr in its composition, due to dilution during deposition and uncontrolled solidification, which generates heterogeneous microstructure and considerable residual stresses.



**Fig 7.** Bar graph with confidence intervals for the microhardness measurements in the MB, ZTA and ZF regions.

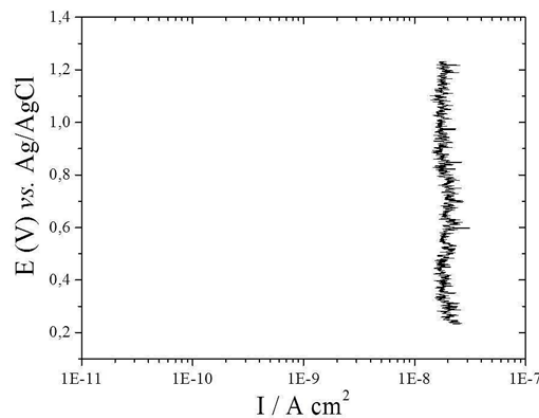
### Corrosion Tests

Figure 8 shows the variation of the open circuit potential with the immersion time of the coating in NACE A TM0177 solution in the aerated condition. The potential initially increases, probably due to the formation of a passive layer that protects the surface, a fact attributed to the high Ni and Cr contents that can form oxides such as NiO and Cr<sub>2</sub>O<sub>3</sub> on the Inconel surface [22]. After 2h, the potential decreases very slowly, probably due to a dissolution process over long immersion times. According to some authors [23,8,24], the electrochemical behavior of Inconel 625 is complex due to the high content of alloying elements such as Cr and Mo.



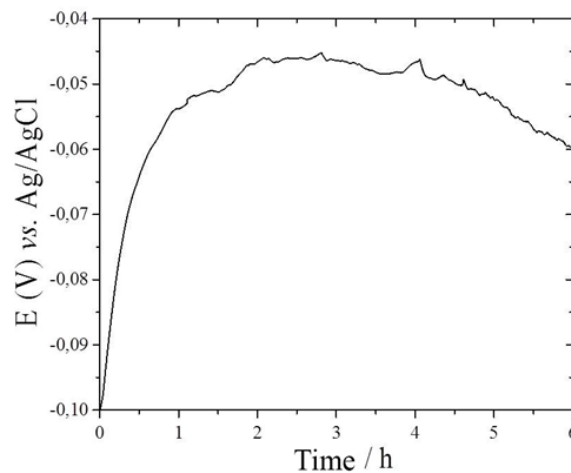
**Fig 8.** Variation of the open circuit potential of the coating in the aerated condition.

The polarization curve obtained in the aerated condition showed a passive behavior with a very low current density ( $< 0.01 \mu\text{A}/\text{cm}^2$ ) (Figure 9). Apparently, a passive layer formed by oxides makes it harder for the coating to dissolve, increasing resistance to corrosion [8].



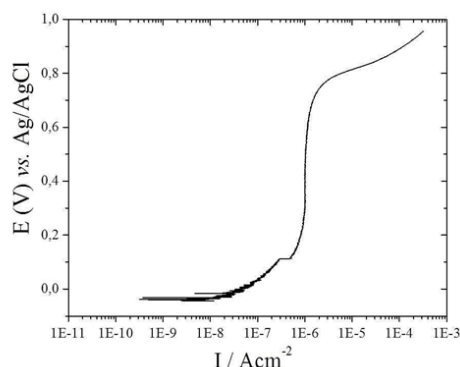
**Fig 9.** Polarization curves of the coating in the aerated condition.

A similar electrochemical behavior was observed in the deaerated medium. In the Figure 10, the potential initially increases, suggesting film formation and growth. After 3.5h, the potential slowly decreases, probably due to a dissolution process. As reported by some authors, the potential measured in open circuit in the deaerated condition reaches an almost stationary state over long immersion times [19-21], which means that the anodic and cathodic reactions of the corrosion reaction no longer change over time.



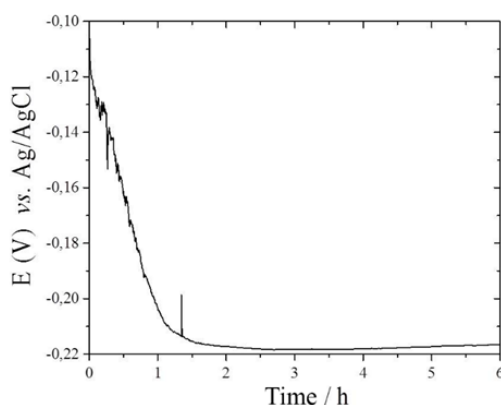
**Fig 10.** Variation of the open circuit potential of the coating in the deaerated condition.

Figure 11 shows the polarization curve, in which it can be seen that in the passive region the current density was around  $1 \mu\text{A}/\text{cm}^2$  over a very wide potential range. From around 0.8 V the passive layer breaks down. According to some authors [25], the Inconel 625 coating exhibits active dissolution behavior and the current density increases constantly when the potential reaches high values in the anodic direction.



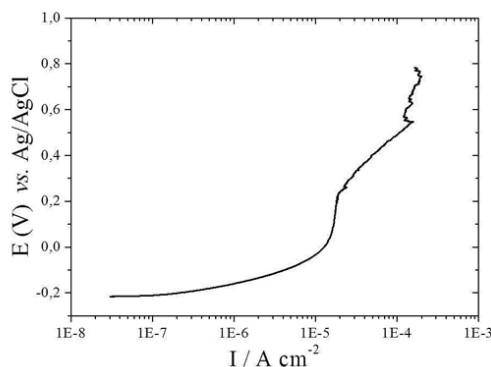
**Fig 11.** Polarization curves of the coating in the deaerated condition.

Figure 12 shows the variation of the open circuit potential with time in the deaerated and  $\text{H}_2\text{S}$  saturated condition. The potential initially decreases and stabilizes after 2 hours, which is probably due to a decrease in the dissolution of the alloy due to the formation of a partially protective film on its surface. In this sense, films formed by precipitation, such as  $\text{NiS}$ ,  $\text{MoS}_2$  and  $\text{FeS}$  are not very adherent, but can act as blockers of the active areas of the surface.



**Fig 12.** Variation of the open circuit potential of the coating in the deaerated condition and with  $\text{H}_2\text{S}$ .

The polarization curve in Figure 13 shows a narrow passive region ( $\sim 0.2 \text{ V}$ ) with a current density of approximately  $2 \times 10^{-5} \text{ A}/\text{cm}^2$ , followed by the breakdown of passivity and the dissolution of the film and coating, which occurs from 0.3 V onwards. As can be seen,  $\text{H}_2\text{S}$  was very aggressive towards the coating, a fact attributed to the presence of  $\text{H}^+$  ions and  $\text{HS}^-$  which make it difficult to form a passive film [26].



**Fig 13.** Polarization curves of the coating in the deaerated condition and with  $\text{H}_2\text{S}$ .

Table 4 shows the corrosion parameters under the different experimental conditions. This table shows the decrease in corrosion potential and the increase in corrosion current density as the aggressiveness of the salt medium increases. Although the corrosion current density is relatively high in the presence of H<sub>2</sub>S, this value is ten times lower than that reported for API 5L X65 steel, used for pipelines, under the same experimental conditions [27].

**Table 4.** Corrosion parameters of the coating in NACE 177A solution.

Condition	E <sub>corr</sub> (V)	I <sub>corr</sub> (A cm <sup>-2</sup> )
Aerated	0,20	1,0X10 <sup>-8</sup>
Deaerated	-0,06	1,0X10 <sup>-6</sup>
Deaerated and Saturated w/ H <sub>2</sub> S	-0,20	2,0X10 <sup>-5</sup>

#### IV. Conclusions

The Inconel coating had a dendritic microstructure with disordered growth directions, characteristic of the manual TIG welding process. Welding the following conclusions:

1. This coating had a significant increase in Fe content throughout its thickness, reaching close to 25% on its surface. In this sense, this coating is not suitable for use in the oil industry, which suggests depositing more than one layer to ensure that the coating composition is no greater than 10%.
2. The coating-substrate interface had no defined morphology. The highest Vickers microhardness values were recorded in this region, probably due to the enrichment of Fe and Cr in its composition and uncontrolled solidification, which generates a heterogeneous microstructure with residual stresses.
3. Electrochemical behavior in aerated media is complex. The presence of oxygen makes the acidic medium more oxidizing, inducing the growth of a protective film.
4. In deaerated media, the passivity current density was 100 times higher than in aerated media. Despite this, the low current densities recorded indicate that the alloy was resistant to corrosion.
5. In a deaerated medium saturated with H<sub>2</sub>S, the electrochemical behavior was completely different. The coating showed lower stability compared to the other experimental conditions. This behavior may be associated with the formation of a poorly adherent and, consequently, poorly protective sulfide film that allows the less noble components of the coating, such as iron, to dissolve.

#### Acknowledgments

The authors would like to thank the Graduate Program in Mechanical Engineering at UNESP Guaratinguetá and CAPES (Coordenação de Aperfeiçoamento de Pessoal de Nível Superior) for the support provided in the form of a master's scholarship during the development of this work.

#### Declaration of authors' contribution

ÉMAA: Conceptualization, formal analysis, research methodology, validation, original document writing, manuscript writing - review and editing. IAF: conceptualization, research and data analysis. RRL: formal analysis, research and writing of the manuscript - review and editing. RBR: data analysis, conceptualization, research, manuscript writing - review and editing. PLF: data analysis. HAA: conceptualization, methodology, research, supervision, data analysis and formal. RZN: data analysis. ENC: conceptualization, methodology, research, final revision of the manuscript and research supervisor.

#### References

- [1]. Leffler, W. L., Sterling, G., & Pattarozzi, R. (2011). *Deepwater Petroleum Exploration & Production: A Nontechnical Guide* (2nd Ed.). Pennwell Corp.
- [2]. Fioravante, I. A., Gomes, J. A. C. P., Bracarense, A. Q., Pessoa, E. C. P., & Liu, S. (2019). Films Formed On Carbon Steel In Sweet Environments—A Review. *Journal Of The Brazilian Chemical Society*, 30(7), 1341–1349. <https://doi.org/10.21577/0103-5053.20190055>
- [3]. Bunaziv, I., Olden, V., & Akselsen, O. M. (2019). Metallurgical Aspects In The Welding Of Clad Pipelines—A Global Outlook. *Applied Sciences*, 9(15), 3118. <https://doi.org/10.3390/app9153118>
- [4]. Frei, J., Alexandrov, B. T., & Rethmeier, M. (2019). Low Heat Input Gas Metal Arc Welding For Dissimilar Metal Weld Overlays Part III: Hydrogen-Assisted Cracking Susceptibility. *Welding In The World*, 63(3), 591–598. <https://doi.org/10.1007/S40194-018-0674-7>
- [5]. Mendes Da Mota, C. A., Souza, D., Lima, M. S. F., & Bracarense, A. Q. (2018). Nickel Overlay Deposited By MIG Welding And Cold Wire MIG Welding. *Welding International*, 32(9), 588–598. <https://doi.org/10.1080/09507116.2017.1347333>
- [6]. Kourdani, A., & Derakhshandeh-Haghighi, R. (2018). Evaluating The Properties Of Dissimilar Metal Welding Between Inconel 625 And 316L Stainless Steel By Applying Different Welding Methods And Consumables. *Metallurgical And Materials Transactions A*, 49(4), 1231–1243. <https://doi.org/10.1007/S11661-018-4469-7>
- [7]. Hernández-Rodríguez, M. L. (2019). Welding Input Effect On The Corrosion Behavior And Microstructure Of Heat Treated GTAW Welds Of Inconel 718. *International Journal Of Electrochemical Science*, 14(5), 4083–4094. <https://doi.org/10.20964/2019.05.43>
- [8]. Tumer, M., Karahan, T., & Mert, T. (2020). Evaluation Of Microstructural And Mechanical Properties Of Dissimilar Inconel 625 Nickel Alloy–UNS S32205 Duplex Stainless Steel Weldment Using MIG Welding. *Welding In The World*, 64(1), 21–35.

- <https://doi.org/10.1007/S40194-019-00825-X>
- [9]. Dai, T., Wang, G., Zhang, D., & Chen, S. (2019). Precipitation Behavior And Hardness Response Of Alloy 625 Weld Overlay Under Different Aging Conditions. *Welding In The World*, 63(4), 1087–1100. <https://doi.org/10.1007/S40194-019-00724-1>
- [10]. Lourenço, J. C., Souza, E. C., Kuri, S. E., & Rovere, C. A. D. (2021). Influence Of The Iron Content On The Microstructure And Electrochemical Behavior Of As-Cast Modified Inconel 625. *Corrosion Science*, 193, 109892. <https://doi.org/10.1016/J.Corsci.2021.109892>
- [11]. Silwal, B., Walker, J., & West, D. (2019). Hot-Wire GTAW Cladding: Inconel 625 On 347 Stainless Steel. *The International Journal Of Advanced Manufacturing Technology*, 102(9–12), 3839–3848. <https://doi.org/10.1007/S00170-019-03448-0>
- [12]. DNV. (2010). \*Offshore Standard DNV-OS-F101: Submarine Pipeline Systems\*. DNV.
- [13]. Mohammadi Zahrani, E., & Alfantazi, A. M. (2021). Hot Corrosion Of Inconel 625 Wrought Alloy And Weld Overlay On Carbon Steel By Gas Metal Arc Welding In 47 Pbso4-23 Zn-13 Pb3O4-7 Pbcl2-5 Cdo-5 Fe2O3 Molten Salt Mixture. *Corrosion Science*, 183, 109348. <https://doi.org/10.1016/J.Corsci.2021.109348>
- [14]. NACE International. (1997). \*TM0177-96: Standard Test Method Laboratory Testing Of Metals For Resistance To Sulfide Stress Cracking And Stress Corrosion Cracking In H2S Environments\*.
- [15]. Lincoln Electric. (2016). *Metrode Welding Consumables* (Pp. 1–23).
- [16]. ASTM International. (2017). *ASTM E3: Standard Guide For Preparation Of Metallographic Specimens*.
- [17]. ASTM International. (2016). \*ASTM E384-11e1: Test Method For Knoop And Vickers Hardness Of Materials\*.
- [18]. Jose, T. A., Araújo, L. S., Souza, J. A., Mendes, M. C., & Dille, J. (2014). Impact Of Dilution On The Microstructure And Properties Of Ni-Based 625 Alloy Coatings. *Soldagem & Inspeção*, 19(2), 134–144. <https://doi.org/10.1590/0104-9224/SI1902.05>
- [19]. Tascheck, B. L., & Da Cunha, T. V. (2022). Prospecting For The Surface Treatment Of A Nickel-Aluminium Bronze Alloy Using The TIG Process. *Soldagem E Inspeção*, 28, E2801. <https://doi.org/10.1016/J.Actamat.2018.03.017>
- [20]. Batista, V. R., Silva, R. H. G., Souza, R. C., & Mendes, M. C. (2021). Efeito Do Tratamento Térmico De Alívio De Tensão E Do Preaquecimento Na Microestrutura E Microdureza Da Interface Entre Depósitos De Inconel 625 E Aços AISI 8630M E AISI 4130. *Matéria (Rio De Janeiro)*, 26(1), E1220. <https://doi.org/10.1590/S1517-707620210001.1220>
- [21]. Narayana Reddy, B., Suresh Kumar, R., & Venkata Rao, D. (2020). Experimental Study Of Laser Beam Welding Process Parameters On AISI 4130-309 Joint Strength. *Materials Today: Proceedings*, 22, 2741–2750. <https://doi.org/10.1016/J.Matpr.2020.03.405>
- [22]. Sandes, S. S., Araújo, L. S., Souza, J. A., Mendes, M. C., & Dille, J. (2016). Avaliação De Revestimentos De Liga De Níquel 625 Depositados Pelo Processo Eletroescória. *Soldagem E Inspeção*, 21(4), 417–427. <https://doi.org/10.1590/0104-9224/SI2104.03>
- [23]. Ge, T., Liu, X., Wang, J., Lin, S., & Chen, L. (2022). Microstructure And Corrosion Resistance Of Tic/Inconel 625 Composite Coatings By Extreme High Speed Laser Cladding. *Optics & Laser Technology*, 150, 107919. <https://doi.org/10.1016/J.Optlastec.2022.107919>
- [24]. Zhang, F., Levine, L. E., Allen, A. J., Stoudt, M. R., Lindwall, G., Lass, E. A., Williams, M. E., Idell, Y., & Campbell, C. E. (2018). Effect Of Heat Treatment On The Microstructural Evolution Of A Nickel-Based Superalloy Additive-Manufactured By Laser Powder Bed Fusion. *Acta Materialia*, 152, 200–214. <https://doi.org/10.1016/J.Actamat.2018.03.017>
- [25]. Xu, L., Wang, Y., Jing, H., Han, Y., & Zhao, L. (2019). Insights Into The Intergranular Corrosion Of Overlay Welded Joints Of X65-Inconel 625 Clad Pipe And Its Relationship To Damage Penetration. *Corrosion Science*, 160, 108169. <https://doi.org/10.1016/J.Corsci.2019.108169>
- [26]. Corrotherm International. (N.D.). *How To Select Corrosion-Resistant Alloys For The Sour Gas And Oil Industry*.
- [27]. Codaro, E. N., Nakazato, R. Z., & Hein, L. R. O. (2018). Corrosion Behavior Of API 5L X65 Steel Subject To Plastic Deformation. *Journal Of Materials Research And Technology*, 7, 314–318. <https://doi.org/10.1016/J.Jmrt.2018.02.006>